Heliyon 10 (2024) e31463

Contents lists available at ScienceDirect

Heliyon

journal homepage: www.cell.com/heliyon

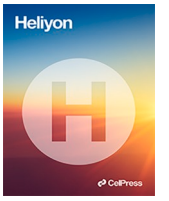

Research article

$TbCu_7$-type Sm-Fe(-N) powder synthesized by low-temperature reduction-diffusion process using the Li–Ca reductant

Jungryang Kim *, Shusuke Okada, Jian Wang, Kenta Takagi, J. Kim **, S. Okada, J. Wang, K. Takagi

Innovative Functional Materials Research Institute, National Institute of Advanced Industrial Science and Technology (AIST), 4-205 Sakurazaka, Moriyama-ku, Nagoya, Aichi 463-8560, Japan

ARTICLE INFO

Keywords:
Low-temperature synthesis
Reduction-diffusion process
Li–Ca alloy
Sm-Fe compounds
Permanent magnets

ABSTRACT

It was predicted that $TbCu_7$-type Sm-Fe powder prepared by the low-temperature reduction-diffusion (LTRD) process using a Li-Ca reductant would contain no residual α-Fe because this reductant would not produce the absorbed water that hinders the reaction between Sm and Fe by forming oxychlorides when molten salt is used as the reductant. Contrary to this expectation, a detailed microstructure analysis revealed that a residual phase of unreacted α-Fe existed in some $TbCu_7$-type Sm-Fe particles rather than as separate Fe particles. This residual α-Fe phase was not located in the center of the Sm-Fe particles and was not detected in some Sm-Fe particles, suggesting that the reason for the residual α-Fe phase is inhomogeneous diffusion of Sm into the Fe due to slow diffusion at low temperatures. Although this $TbCu_7$-type Sm-Fe powder contained a small amount of unreacted α-Fe phase, the magnetic properties of the nitride $TbCu_7$-type Sm-Fe were also estimated.

1. Introduction

Permanent magnets are used in motors in various fields such as electric vehicles (EVs), home appliances, and wind power generation, among others. Efforts to completely replace gasoline-powered vehicles with EVs are now underway, as environmental problems become more serious and social needs require research on environment-friendly technologies to realize energy saving and ultimately, carbon neutrality. Therefore, it is essential to develop motors with the highest possible efficiency, and the development of a high-performance permanent magnet will be an indispensable part of this effort. Since the development of the Nd-Fe-B magnet as the highest-performance permanent magnet in 1984 [1], this type has become the most widely used magnet in commercial applications. Because the present Nd-Fe-B magnet has problems such as an unstable supply, which increases costs, and low thermal stability, other permanent magnets that surpass the Nd-Fe-B magnet are being actively developed, but none has yet reached the stage of practical application.

As a "post Nd-Fe-B magnet," the $TbCu_7$-type $(Sm,Zr)(Fe,Co)_{10}N_y$ magnet with magnetic properties of magnetization saturation $J_s = 1.7$ T, anisotropy field $H_a = 7.7$ T and Curie temperature $T_C = 520$ °C [2] is one candidate for surpassing the Nd-Fe-B magnet ($J_s = 1.6$ T, $H_a = 7.6$ T, $T_C = 312$ °C) [1,3,4]. $TbCu_7$-type $SmFe_x$-based magnets can have $x = 8.5$ to 10 stoichiometrically, and their saturation

* Corresponding author
** Corresponding author.
E-mail address: jungryang.kim@aist.go.jp (J. Kim).

https://doi.org/10.1016/j.heliyon.2024.e31463
Received 29 February 2024; Received in revised form 15 May 2024; Accepted 16 May 2024
Available online 16 May 2024

magnetization increases with higher Fe contents. Although Sakurada et al. succeeded in achieving $x = 10$, other problems remained [2]. Normally, an anisotropic magnet, in which the magnetic moments are aligned in the same direction, is necessary for a high-performance permanent magnet in the bulk state, and anisotropic magnets can be produced from single-crystalline powder. Among various synthesis methods for $TbCu_7$-type Sm-Fe based magnets, such as melt spinning [2,5–11], the hydrogenation-disproportionation-desorption-recombination process [12–14], mechanical alloying [15–17], and the low-temperature reduction-diffusion (LTRD) process [18–22], only the LTRD process is capable of producing a raw single-crystalline powder for an anisotropic magnet. It is well known that the reduction-diffusion (RD) process can synthesize single-crystalline $Sm_2Fe_{17}N_z$ magnetic powder by reduction of samarium oxide using Ca as a reductant (Sm_2O_3 (s) + 3Ca (l) → 2Sm + 3CaO) and diffusion of Sm atoms to Fe particles through liquid Ca at a temperature over 850 °C, which is the melting point of Ca [23–30]. Our group successfully synthesized single-crystalline $TbCu_7$-type Sm-Fe by the LTRD process using LiCl molten salt as a solvent for Ca to decrease the reaction temperature, which is limited to the melting point of Ca [18]. Since the melting point of LiCl is approximately 600 °C, Ca could be dissolved in liquid LiCl at a temperature below its melting point. In this process, $SmCl_3$ was used as a precursor because it is also a chloride with molten salt and is liquefied with the molten salt to increase reactivity even at low temperatures ($2SmCl_3$ (l) + 3Ca (in LiCl melt) → 2Sm + $3CaCl_2$). However, it was not possible to obtain a single-phase $TbCu_7$-type Sm-Fe powder because the product included an unreacted α-Fe phase. Okada et al. suggested that this residual unreacted α-Fe phase remained because oxychlorides [18], which originate from the water absorbed in chlorides and are insoluble in a chloride molten salt [31–33], covered the Fe particles, inhibiting the diffusion of Sm to Fe. Sato et al. continued to use molten salt in the LTRD process but used metallic Sm as the Sm precursor instead of $SmCl_3$ [20]. In this case. the amount of residual α-Fe was decreased, but the residual α-Fe phase was not completely eliminated.

Meanwhile, in our previous study, we used a Li–Ca eutectic melt as a reductant in the LTRD process [22]. Li has a eutectic point with Ca at around 230 °C and does not react with Sm and Fe, which means Ca can be liquified at a low temperature by introducing only Li in the conventional RD process (Sm_2O_3 (s) + 3 Li–Ca (l) → 2Sm + 3CaO + 3Li). Thermodynamically, Li cannot reduce Sm_2O_3 [34]. Since this LTRD process using the Li–Ca reductant does not include chlorides, it was thought that this approach would improve the water problem, which is expected to cause residual Fe if molten salts are used. Therefore, in the present study, we investigate the possibility of producing a single-phase $TbCu_7$-type Sm-Fe powder containing no residual Fe by the LTRD process using the Li–Ca reductant. In addition, the magnetic properties of the Sm-Fe-N powder obtained by nitriding the produced $TbCu_7$-type Sm-Fe powder are also reported.

2. Experimental method

The entire LTRD process is the same as that used in the previous experiment [22] and consists of 7 steps: (1) Preparation of the Li–Ca eutectic melt, (2) mixing of the Li–Ca and precursors (α-Fe and Sm_2O_3 powders), (3) heat treatment, (4) crushing, (5) nitriding, (6) washing, and (7) dehydration. Li granules (1–6 mm, Alfa Aesar Co.) and Ca granules (16 mesh, Alfa Aesar Co.) were mixed at a 1 : 1 M ratio at 350 °C in an iron crucible under Ar with stirring using a low-oxygen fusing system developed by the authors in our previous our research [22], and a uniform liquid Li–Ca melt was produced. Then, the Li–Ca in the iron crucible was mixed with α-Fe and Sm_2O_3 (FUJIFILM Wako Pure Chemical Corp.) using the low-oxygen fusing system at 250 °C, which is slightly higher than the melting point of the Li–Ca alloy (230 °C). The molar ratios of the Li–Ca reductant/precursors examined in this study were 7.8, 9.8, and 11.7. The α-Fe powder was prepared by hydrogen reduction of hematite, as explained in detail in our previous research [19,28]. Next, the prepared iron crucibles were covered with iron lids and heat-treated at various temperatures for 10 h under Ar. The products were washed using ethanol and distilled water several times to remove the residual Li–Ca and Li and CaO product and then dried in a vacuum. (It was estimated that the residual Li–Ca and Li and CaO are almost removed by compositional analysis. See Supporting Information, Fig. S1) Hydrogen gas generated during the washing process was diffused into the $TbCu_7$-type Sm-Fe alloy lattice [27], and to remove interstitial hydrogen atoms the washed powders were dehydrogenated at 200 °C for 3 h in a vacuum.

The phases of the synthesized powders were identified by X-ray diffractometry (XRD, PANalytical, Empyrean, CoKα radiation). A Rietveld analysis of the XRD patterns was performed using a HighScore Plus (Malvern Panalytical Ltd.) [35]. The microstructure, composition, and elemental distribution of the particles were analyzed by scanning transmission electron microscopy (STEM) observation and energy dispersive X-ray spectroscopy (EDS) mapping with an atomic-resolution analytical electron microscope (JEM-ARM200F, JEOL Ltd., Tokyo, Japan). Specimens for STEM observation were prepared using a Ga-focused ion beam (Scios, an FEI Versa 3D system). The particle appearance and size were also evaluated with a field-emission scanning electron microscope (FE-SEM, JEOL, JSM-7800F).

In order to estimate the magnetic properties of the samples, the LTRD products before washing were crushed by hand-milling for nitriding. Nitriding was conducted at 320 °C for 1.5 h in a mixed gas of NH_3–H_2-Ar with a 1 : 2: 2 vol ratio, followed by washing and dehydrogenation. The magnetic properties of the synthesized powders were then measured using a vibrating sample magnetometer (VSM, DynaCool, Quantum Design, Inc.) with a maximum applied field of 7.2 $MA{\cdot}m^{-1}$ (90 kOe) in a vacuum at room temperature. For the VSM analysis, the powder particles were uniformly embedded in epoxy resin by orientation under a static magnetic field of 1.6 $MA{\cdot}m^{-1}$ (20 kOe) in order to measure the magnetic properties along the parallel (easy axis) and perpendicular (hard axis) to the aligned direction. The maximum energy product $(BH)_{max}$ value given in the following refers to the theoretical density of 7.72 $g{\cdot}cm^{-3}$, which is calculated from the unit cell of the $TbCu_7$-type Sm-Fe-N compound in this study (see Supporting Information).

3. Results and discussion

3.1. Optimization of LTRD conditions for synthesis of single-phase $TbCu_7$-type Sm-Fe powder

In this study, we introduced the LTRD process using a Li–Ca reductant with Sm_2O_3, which does not use molten salts and a $SmCl_3$ precursor to address the problem of residual water. Also, we optimized the conditions of the LTRD process to produce a single-phase $TbCu_7$-type Sm-Fe powder by predicting various problems related to the residual Fe. Since it can be thought that the reason for the remaining unreacted Fe is an insufficient amount of Sm to react with α-Fe, the ratio of Sm to α-Fe was changed as shown in Fig. 1a, which shows the XRD patterns of the powders synthesized at 600 °C for 10 h depending on the Sm molar ratio. The α-Fe phase gradually decreased as the Sm ratio increased and disappeared at the largest Sm ratio. However, a $SmFe_3$ phase begins to be produced at the Sm ratio of 36 %, and the powder is almost entirely composed of the $SmFe_3$ phase without any $TbCu_7$-type Sm-Fe phase at the largest Sm ratio. The formation of the $SmFe_3$ phase, which is a Sm-rich phase, means that excess Sm was supplied. This phenomenon was investigated in our previous studies [21,22]. Although the amount of α-Fe phase decreased and the α-Fe phase disappeared as the amount of Sm increased, it was found that excessive Sm addition resulted in the formation of a Sm-rich phase, which causes a decrease in saturation magnetization [36]. Therefore, the Sm ratio that achieves the smallest amount of the α-Fe phase without the formation of the $SmFe_3$ phase should be selected.

The amount of reductant was also considered. In the LTRD reaction, Sm oxide is reduced in a liquid-state reductant, which is the Li–Ca eutectic melt in this study, and the reduced Sm diffuses through the melt and reacts with the Fe particles. At this time, a certain amount of Sm is lost by the dissolution of the reduced Sm in the reductant melt [21], but Sm exceeding solubility may cause a reaction with Fe. Therefore, the reaction of Sm and Fe can be affected by the ratio of the reductant and reactant because the amount of reduced Sm depends on the amount of Li–Ca liquid. The amount of Li–Ca reductant was changed as shown in Fig. 1b, which shows the XRD patterns of the powders synthesized at 600 °C for 10 h using 30 % Sm. At the largest amount of Li–Ca reductant, the largest amount of unreacted α-Fe phase remained, while the smallest amount of Li–Ca reductant also resulted in a larger amount of unreacted α-Fe phase than an intermediate amount of Li–Ca reductant. The former means that too much Sm was dissolved in the large amount of Li–Ca melt and the amount of Sm that did not react with Fe increased, resulting in an insufficient supply of Sm. The latter implies that the overall

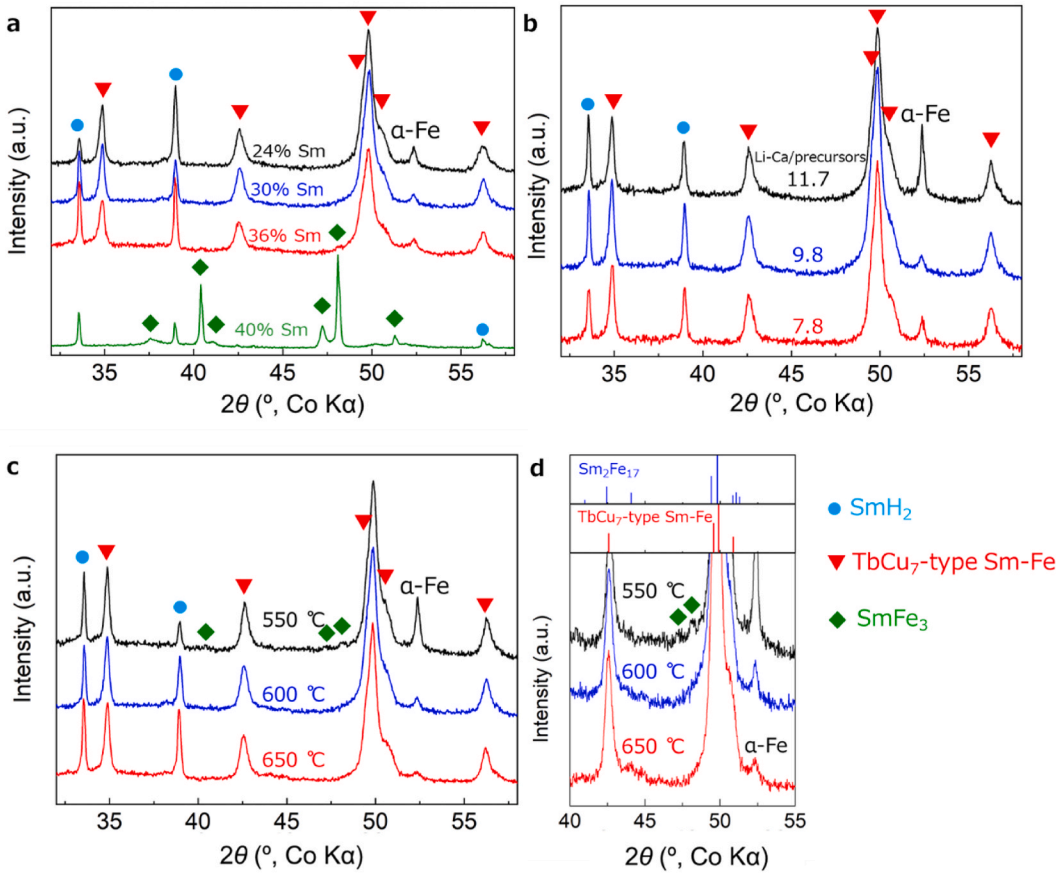

Fig. 1. XRD patterns of powders synthesized by the LTRD process depending on **a** Sm molar ratio vs. α-Fe, **b** molar ratio of Li–Ca reductant/precursors and, **c** processing temperatures. **d** is an enlarged view of (c) of the range between 40° and 55°.

amount of Sm that can be reduced decreases as the amount of reductant decreases, and the amount of Sm that exceeds solubility in the Li–Ca melt is not sufficient to react with all the Fe powder. As evidence for the dissolution of Sm in the reductant, Fig. 1 also shows SmH_2 peaks; these are the result of hydrogenation of residual Sm by hydrogen generated by oxidation of the reductant during the washing process [20] and remain in the powder because its decomposition temperature is over 700 °C in vacuum [37].

Since the diffusion rate in the LTRD process affects the reaction, the effect of temperature changes was also investigated, as shown in Fig. 1c and d. The powder synthesized at 550 °C includes a large amount of α-Fe phase and a small amount of $SmFe_3$. Because this $SmFe_3$ phase could be eliminated at over 600 °C by using an appropriate Sm/Fe ratio [22], this means the $TbCu_7$-type Sm-Fe phase synthesis reaction was not complete. On the other hand, the powder synthesized at 650 °C shows the smallest amount of the α-Fe phase but also includes the Sm_2Fe_{17} phase. As can be seen in Fig. 1d, which shows the enlarged XRD patterns between 40° and 55°, the XRD peak at about 44° represents the superlattice of the Sm_2Fe_{17} phase, which begins to appear at 650 °C, indicating that the formation of the Sm_2Fe_{17} phase begins from 650 °C. Therefore, 600 °C is the optimum temperature for synthesizing the $TbCu_7$-type Sm-Fe phase, even though a small amount of α-Fe phase will remain.

As a result of considering the synthesis of only the $TbCu_7$-type Sm-Fe phase without other Sm-Fe phases such as $SmFe_3$ and Sm_2Fe_{17}, the α-Fe phase finally remained, albeit in a small amount of 3.5 wt%, which was calculated by a Rietveld analysis using the XRD peak of the Sm-Fe powder including the smallest amount of Fe (blue peak in Fig. 1). Although this amount of residual α-Fe phase is smaller than in the LTRD process using molten salts (see Supporting Information, Fig. S2), this result implies that the residual Fe may also be caused by factors other than the oxychloride originating from the water problem. In order to understand the origin of the residual Fe in this study, it is necessary to investigate the phase state of the Fe in the produced powder to clarify whether the residual Fe existed separately or inside the $TbCu_7$-type Sm-Fe particles.

3.2. *Microstructures of $TbCu_7$-type Sm-Fe particles*

To investigate the state of the residual α-Fe phase in the synthesized powder, cross-sectional observation of the particles was

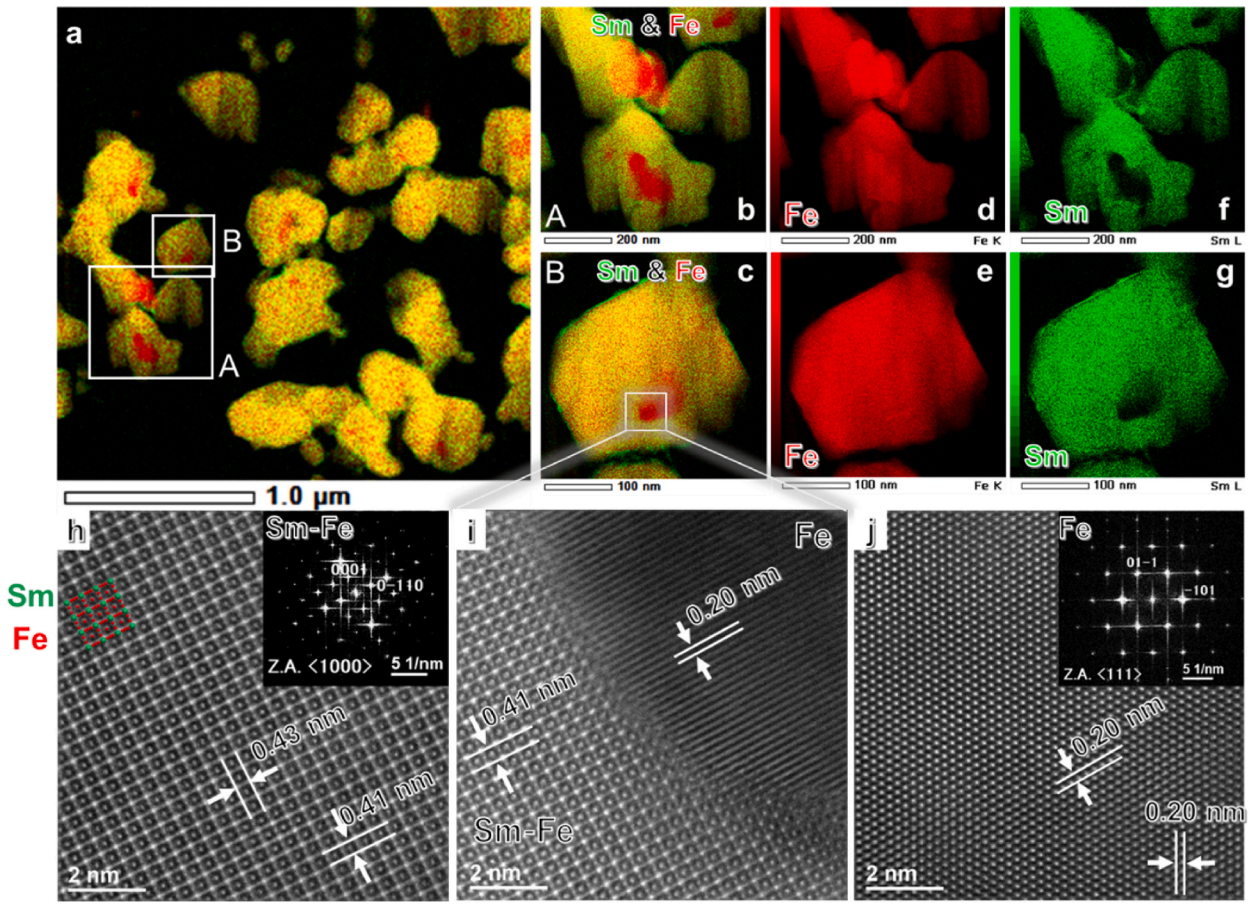

Fig. 2. EDS element distribution mapping images of **a-c** combined elements (Fe and Sm), **d-e** Fe, and **f-g** Sm in particles in the powder synthesized at 550 °C. High-resolution HAADF-STEM images focusing on the detailed microstructure of **h** $TbCu_7$-type phases, **i** $TbCu_7$-type Sm-Fe/Fe interface (indicated by the white square in **c**) and, **j** α-Fe phase.

performed by EDS element mapping and high-resolution STEM characterization, as shown in Fig. 2 (synthesis at 550 °C) and in Fig. 3 (600 °C). As the element mappings in Fig. 2a–g indicate, some of the individual powder particles synthesized at 550 °C contain a Fe-rich phase (red color in Fig. 2a–c) within a homogeneous Sm-Fe intermetallic compound (orange (yellow)-like color, which shows Sm and Fe atoms were homogeneously mixed in Fig. 2a–c). Fig. 2h presents a high-resolution HAADF-STEM image taken from the <1000> zone axis of the Sm-Fe phase region near the boundary in Fig. 2c. With a distinct atomic number between Sm and Fe, the brighter atoms in Fig. 2h indicate Sm, while the darker ones are Fe atoms (as show in the crystal model inset in Fig. 2h). A metastable $TbCu_7$-type Sm-Fe phase was identified by calculating the lattice constants from the high angle angular dark field (HAADF)-STEM image ($d_{0001} = 0.41$ nm, $d_{0\text{-}110} = 0.43$ nm), and indexing and matching the spots in the corresponding FFT (inset in Fig. 2h). Using a similar method, the Fe region was identified as the α-Fe phase (Fig. 2j), in which $d_{01\text{-}1} = d_{\text{-}101} = 0.20$ nm. Fig. 2i shows the detailed microstructure at the Sm-Fe/Fe interface, which reveals some degree of epitaxial relationship between the α-Fe phase and the $TbCu_7$-type Sm-Fe phase, that is, $(011)_{Fe}//(0001)_{S\text{-}Fe}$. This type of epitaxial relationship is energy favorable due to its close lattice spacing (as shown in Fig. 2i), which leads to a small lattice misfit (3.4 %) and thus lower strain/interfacial energy. This implies that the formation of the $TbCu_7$-type Sm-Fe phase is dominated by the diffusion of Sm atoms into the α-Fe lattice during the LTRD process and that this diffusion does not require high energy.

The powder synthesized at 600 °C consists almost entirely of single $TbCu_7$-type Sm-Fe particles and some Sm-Fe particles containing the α-Fe phase within the particles, as can be seen in Fig. 3. Fig. 3c and d show the overlapped Fe and Sm element mapping images of a single $TbCu_7$-type Sm-Fe particle (A in Fig. 3b) and a particle including Fe (B in Fig. 3b). The Fe region is considered to be a pure α-Fe phase because its lattice parameter is the same as that in the case of 550 °C, as can be seen in Fig. 3e. This Fe region is smaller than at 550 °C. It is implied that the Sm-Fe region at 600 °C becomes thicker than at 550 °C due to greater diffusion of Sm into Fe because the higher processing temperature accelerates interdiffusion between Sm and Fe. This also implies that the formation of the metastable $TbCu_7$-type Sm-Fe product phase is dominated by the diffusion of Sm into Fe.

One interesting finding from these microstructural observation results is that most residual α-Fe phases are not located in the center of the Sm-Fe particles, as shown in Figs. 2 and 3. This means that the reduced Sm was not supplied homogeneously. Comparing the powders synthesized at 600 °C and 650 °C in Section 3.1, the amount of the residual α-Fe phase decreased greatly at 650 °C. This suggests that the diffusion rate increases as the temperature increases, and Sm is supplied effectively at higher temperatures regardless of the homogeneity of Sm supply. The uniformity of the reactants is not a major problem in the conventional RD process, which is conducted at over 850 °C and produces no residual α-Fe phase [26]. However, because the LTRD process is performed at a significantly

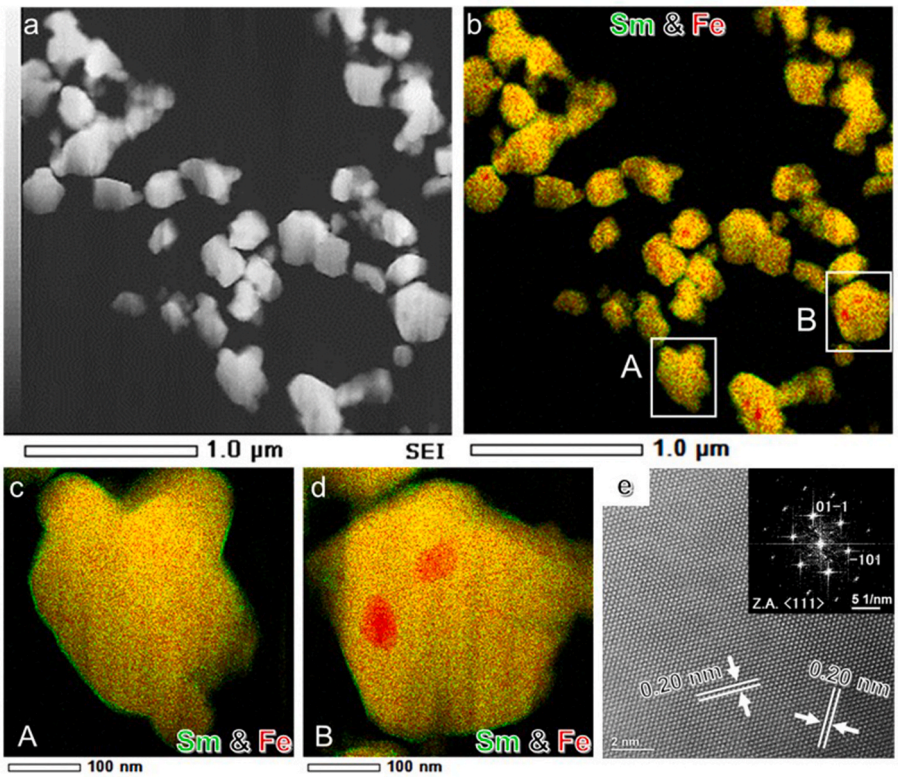

Fig. 3. **a** SEI-STEM image and corresponding distribution mapping images of **b-d** combined elements (Fe and Sm) in particles in the powder synthesized at 600 °C. The observed areas are indicated by the white squares denoted A and B in **b**. **e** High-resolution HAADF-STEM image focusing on the detailed microstructure of the Fe-rich region.

lower temperature, dependence on the homogeneity of Sm supply increases as the diffusion rate decreases. This implies that $TbCu_7$-type Sm-Fe phases with or without the residual α-Fe phase would be produced inhomogeneously, and the residual α-Fe phases would not be located in the center of the Sm-Fe particles. This homogeneity was independent of the LTRD time. Actually, the amount of residual α-Fe phase did not decrease when the LTRD time was increased from 10 h to 50 h (600 °C) (see Supporting Information, Fig. S3), and it seems that the diffusion (supply) of Sm atoms to the α-Fe phase stopped. Therefore, in order to mix Sm and Fe homogeneously, it is necessary to improve the LTRD process, *i.e.*, by utilizing a stirring reaction or homogenously-mixed precursors and so on.

The mean particle diameter of the $TbCu_7$-type Sm-Fe powder was estimated as 354 nm as can be seen in Fig. 4a and b. To the best of our knowledge, this particle size is the smallest among those reported for the other Sm-Fe powders synthesized by the LTRD process using molten salts [18–20].

3.3. Magnetic properties of $TbCu_7$-type Sm-Fe-N powders

Nitriding was applied to the Sm-Fe powder with the smallest amount of α-Fe, which was synthesized at 600 °C for 10 h. The amount of α-Fe after nitriding was calculated as approximately 1.7 wt% by a Rietveld analysis using the XRD pattern shown in Fig. 5a. As seen in the inset SEM image in Fig. 5a, the primary particle size did not change significantly after nitriding, even though agglomeration of some particles occurred during the nitriding process. Fig. 5b shows the magnetic curves of the $TbCu_7$-type Sm-Fe-N powder. Magnetization at 7.2 MA m^{-1} ($\sigma_{@7.2\ MA\cdot m\text{-}1}$), remanence magnetization along the easy axis ($\sigma_{r\text{-}easy}$) and hard axis ($\sigma_{r\text{-}hard}$), coercivity (H_c), and maximum energy product $(BH)_{max}$ were 92.9 $Am^2\cdot kg^{-1}$, 49.9 $Am^2\cdot kg^{-1}$, 44.2 $Am^2\cdot kg^{-1}$, 5.5 $MA\cdot m^{-1}$, and 95.89 $kJ\cdot m^{-3}$, respectively. Magnetization is not particularly high for the following two reasons: 1. The specimens contained impurities such as Sm_2O_3 and SmH_2 (Fig. 5a), which can be removed by acid treatment, and 2. the $SmFe_xN_y$ used in this study is not a Fe-rich $TbCu_7$-type Sm-Fe phase. Normally, $TbCu_7$-type $SmFe_xN_y$ has a nonstoichiometric structure, and the Fe content, x, can be increased by the substitution of Sm sites for pairs of Fe atoms (Fe dumbbells). Magnetization can be increased by increasing the Fe content (Fe-rich $TbCu_7$-type Sm-Fe phase). The value of c/a is used to predict the Fe content, as c/a increases with the Fe content. The lattice parameters of the Sm-Fe-N phase were calculated as $a = 0.5037$ nm and $c = 0.4242$ nm. The c/a of 0.842 obtained in this study is slightly larger than the 0.839 of $SmFe_{8.5}N_{1.5\text{-}1.9}$ [17] and smaller than the 0.859 of $(Sm_{7.80}Zr_{1.05})(Fe_{75.00}Co_{3.96})N_{12.19}$ [9], in which x = approximately 8.9. Therefore, the Fe content of the $SmFe_xN_y$ in this study is close to 8.5 or slightly higher, and high magnetization could not obtained. To increase magnetization, it is necessary to synthesize a Fe-rich Sm-Fe-N powder by substituting another element such as Zr or Co and so on. The degree of alignment (DoA) is estimated as follows using $\sigma_{r\text{-}easy}$ and $\sigma_{r\text{-}hard}$:

$$DoA(\%) = \frac{\sigma_{r-easy} - \sigma_{r-hard}}{\sigma_{r-easy}} \times 100 \quad (1)$$

The calculated DoA is 11.4 %. In this study, $\sigma_{@7.2\ MA\cdot m\text{-}1}$ is lower and H_c and DoA are higher than those of the $TbCu_7$-type Sm-Fe-N

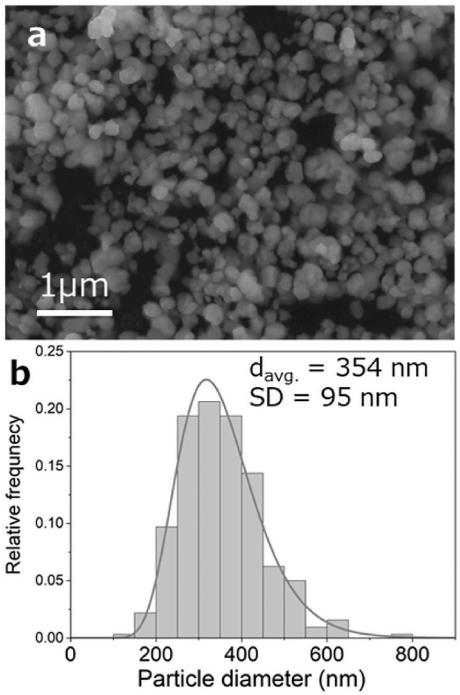

Fig. 4. **a** SEM image and **b** particle size distribution of $TbCu_7$-type Sm-Fe powders synthesized at 600 °C.

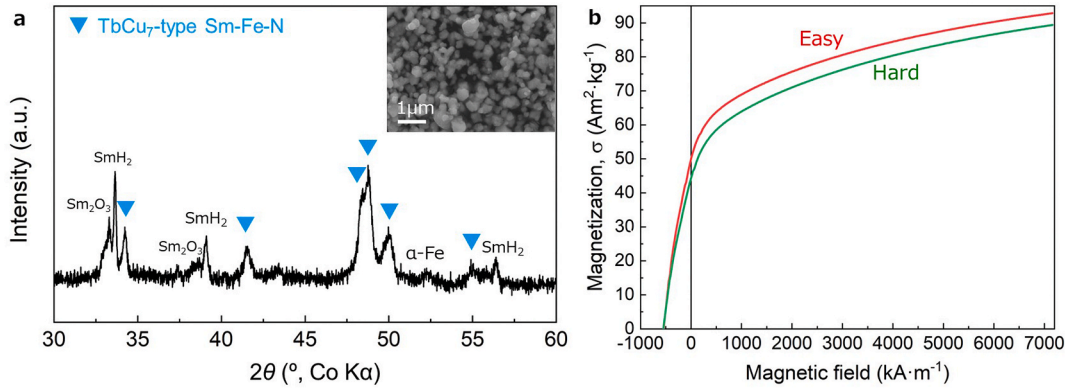

Fig. 5. **a** XRD pattern (inset SEM image) and **b** magnetic curves (room temperature) of easy and hard axes of $TbCu_7$-type Sm-Fe-N powder.

synthesized using molten salts ($\sigma_{@7.2\ MA\cdot m\text{-}1} = 136.3\ Am^2\cdot kg^{-1}$, $H_c = 5.0\ MA\cdot m^{-1}$, *DoA* before milling = 8 %) reported by Sato et al. [20]. Sato et al. increased *DoA* to 22 % by milling the powders because the synthesized powder contained polycrystalline particles. This means the number of single-crystalline particles was increased by crushing the poly-crystalline particles, and suggests the possibility that the *DoA* of our powder can also be increased by milling. In this study, the kink in the magnetic curve in Fig. 5b was not observed. Normally, kinks in magnetic curves (demagnetization curves) are caused by the presence of a soft magnetic phase such as the α-Fe phase [38]. Although a trace amount of the α-Fe phase remained in our powder, its effect did not appear in the magnetic curve. Therefore, no significant problems with the magnetic properties of the materials are expected, even if the powder contains this amount of α-Fe phase.

4. Conclusion

The possibility of synthesizing a single-phase $TbCu_7$-type Sm-Fe powder by a chloride-free LTRD process was investigated. Because the conventional LTRD process using molten salts and chloride precursors has a high probability of causing water absorption, oxychloride is formed. This oxychloride was considered to be a problem, as it hinders the reaction between Sm and Fe, resulting in a residual unreacted α-Fe phase. To solve this problem, a Li–Ca eutectic melt was used as the reductant in this study. By optimizing conditions such as the Sm-Fe ratio, reductant/precursor ratio and, processing temperature, the α-Fe phase could be decreased to as low as 3.5 wt%. Although some residual α-Fe phase remains, this is smaller than in the LTRD process using molten salts. An analysis of the microstructure of the powders revealed that some $TbCu_7$-type Sm-Fe particles contained α-Fe phases, which were not located in ther center of the Sm-Fe particles. It is inferred that the reduced Sm was inhomogeneously diffused into the Fe, and some $TbCu_7$-type Sm-Fe particles containing the residual α-Fe phase were not supplied with sufficient Sm. It was newly found that the homogeneity of the reactants becomes an important factor in the LTRD process, which is conducted at lower temperatures and has a slower diffusion rate than the conventional RD process. The magnetic properties of the $TbCu_7$-type Sm-Fe-N powder were estimated by nitriding as $H_c = 5.5\ MA\cdot m^{-1}$, $(BH)_{max} = 95.89\ kJ\cdot m^{-3}$, and $DoA = 11.4$ %.

Funding

This research was in part supported by “The Naito Research Grant (The Naito Science and Engineering Foundation)”.

Data availability statement

The data that has been used is confidential.

CRediT authorship contribution statement

Jungryang Kim: Writing – original draft, Visualization, Validation, Software, Methodology, Investigation, Formal analysis, Data curation, Conceptualization. **Shusuke Okada:** Writing – review & editing, Supervision, Conceptualization. **Jian Wang:** Writing – review & editing, Visualization. **Kenta Takagi:** Writing – review & editing, Supervision, Conceptualization.

Declaration of competing interest

The authors declare the following financial interests/personal relationships which may be considered as potential competing interests:Jungryang Kim reports financial support was provided by The Naito Science and Engineering Foundation. If there are other authors, they declare that they have no known competing financial interests or personal relationships that could have appeared to influence the work reported in this paper.

Acknowledgments

The authors wish to express their appreciation to Kazumi Hayakawa for technical assistance with the micro-sample preparation by FIB (focused ion beam) milling.

Appendix A. Supplementary data

Supplementary data to this article can be found online at https://doi.org/10.1016/j.heliyon.2024.e31463.

References

[1] M. Sagawa, S. Fujimura, N. Togawa, H. Yamamoto, Y. Matsuura, New material for permanent magnets on a base of Nd and Fe, J. Appl. Phys. 55 (6) (1984) 2083–2087, https://doi.org/10.1063/1.333572.
[2] S. Sakurada, A. Tsutai, T. Hirai, Y. Yanagida, M. Sahashi, S. Abe, T. Kaneko, Structural and magnetic properties of rapidly quenched (R,Zr)(Fe,Co)$_{10}$N$_x$(R= Nd, Sm), J. Appl. Phys. 79 (8) (1996) 4611–4613, https://doi.org/10.1063/1.361679.
[3] A. Manaf, R.A. Buckley, H.A. Davies, New nanocrystalline high-remanence Nd-Fe-B alloys by rapid solidification, J. Magn. Magn Mater. 128 (3) (1993) 302–306, https://doi.org/10.1016/0304-8853(93)90475-H.
[4] Y. Matsuura, Recent development of Nd–Fe–B sintered magnets and their applications, J. Magn. Magn Mater. 303 (2) (2006) 344–347, https://doi.org/10.1016/j.jmmm.2006.01.171.
[5] M. Katter, J. Wecker, L. Schultz, Structural and hard magnetic properties of rapidly solidified Sm–Fe–N, J. Appl. Phys. 70 (6) (1991) 3188–3196, https://doi.org/10.1063/1.349302.
[6] T. Yoneyama, T. Yamamoto, T. Hidaka, Magnetic properties of rapidly quenched high remanence Zr added Sm–Fe–N isotropic powders, Appl. Phys. Lett. 67 (21) (1995) 3197–3199, https://doi.org/10.1063/1.115161.
[7] R. Omatsuzawa, K. Murashige, T. Iriyama, Magnetic properties of TbCu$_7$-type Sm-Fe-N melt-spun ribbons, Trans. Magn. Soc. Jpn. 4 (4–1) (2004) 113–116, https://doi.org/10.3379/tmjpn2001.4.113.
[8] C. Lu, X. Hong, Z. Ding, J. Shi, X. Bao, X. Gao, J. Zhu, Phase formation and magnetic hardening mechanism of TbCu$_7$ type Sm-Fe-N powders, J. Magn. Magn Mater. 456 (2018) 6–10, https://doi.org/10.1016/j.jmmm.2018.01.071.
[9] J. Coey, P. Stamenov, S. Porter, M. Venkatesan, R. Zhang, T. Iriyama, Sm-Fe-N revisited; remanence enhancement in melt-spun Nitroquench material, J. Magn. Magn Mater. 480 (2019) 186–192, https://doi.org/10.1016/j.jmmm.2019.02.076.
[10] N. Kurokawa, M. Matsuura, S. Sakurada, S. Sugimoto, Enhancement of magnetic properties and microstructural changes in TbCu$_7$-type Sm-Fe-Co-Nb-B melt-spun ribbons, J. Magn. Magn Mater. 556 (2022) 169414, https://doi.org/10.1016/j.jmmm.2022.169414.
[11] N. Kurokawa, M. Matsuura, S. Sakurada, S. Sugimoto, Effects of Nb and B addition on intrinsic magnetic properties and phase of TbCu$_7$-type Sm-Fe-Co-Nb-B alloys. 2023 IEEE International Magnetic Conference-Short Papers (INTERMAG Short Papers), 2023, pp. 1–2, https://doi.org/10.1109/INTERMAGShortPapers58606.2023.10228543.
[12] C.N. Christodoulou, T. Takeshita, Sm$_2$Fe$_{17}$-nitride-based permanent magnets produced by the hydrogenation-decomposition-desorption-recombination (HDDR) process, J. Alloys Compd. 196 (1–2) (1993) 155–159, https://doi.org/10.1016/0925-8388(93)90587-D.
[13] X.-g. Zhao, Z.-d. Zhang, W. Liu, Q.-f. Xiao, X. Sun, Structural and magnetic properties of Sm-Fe-N magnets prepared by hydrogenation and nitrogenation processes, J. Magn. Magn Mater. 148 (3) (1995) 419–425, https://doi.org/10.1016/0304-8853(95)00021-6.
[14] K. Takagi, M. Jinno, K. Ozaki, Preparation of TbCu$_7$-type Sm-Fe powders by low-temperature HDDR treatment, J. Magn. Magn Mater. 454 (2018) 170–175, https://doi.org/10.1016/j.jmmm.2018.01.092.
[15] O. Mao, J. Yang, Z. Altounian, J.O. Ström-Olsen, Metastable RFe$_7$ compounds (R= rare earths) and their nitrides with TbCu$_7$ structure, J. Appl. Phys. 79 (8) (1996) 4605–4607, https://doi.org/10.1063/1.361739.
[16] A. Teresiak, M. Kubis, N. Mattern, M. Wolf, K.-H. Müller, Formation of modified TbCu$_7$ and Th$_2$Zn$_{17}$ type structures during annealing of mechanical-alloyed Sm–Fe powders, J. Alloys Compd. 274 (1–2) (1998) 284–293, https://doi.org/10.1016/S0925-8388(98)00571-4.
[17] A. Teresiak, M. Kubis, N. Mattern, M. Wolf, W. Gruner, K.-H. Mueller, Influence of nitrogenation on structure development and magnetic properties of mechanically alloyed and annealed Sm–Fe powders, J. Alloys Compd. 292 (1–2) (1999) 212–220, https://doi.org/10.1016/S0925-8388(99)00297-2.
[18] S. Okada, K. Takagi, Novel synthesis of single-crystalline TbCu$_7$ type Sm-Fe powder by low-temperature reduction-diffusion process using molten salt, J. Rare Earths 40 (7) (2022) 1126–1133, https://doi.org/10.1016/j.jre.2021.05.017.
[19] J. Kim, S. Okada, K. Takagi, TbCu$_7$-type Sm-X-Fe compounds (X= Zr, Hf, Y, Dy, La, Ce and Nd) synthesized by low-temperature reduction-diffusion (LTRD) process using molten salt, AIP Adv. 12 (3) (2022) 035306, https://doi.org/10.1063/9.0000283.
[20] S. Sato, K. Nishikawa, E. Node, S. Okada, Development of TbCu$_7$-type Sm-Fe-N anisotropic magnet powder and its sintered magnets, J. Alloys Compd. 929 (2022) 167280, https://doi.org/10.1016/j.jallcom.2022.167280.
[21] J. Kim, S. Okada, K. Takagi, Low-temperature synthesis of Sm-Fe binary compounds by reduction-diffusion process using an eutectic salt solvent, Rare Met. (2023), https://doi.org/10.1007/s12598-022-02219-3.
[22] J. Kim, S. Okada, K. Takagi, Low temperature synthesis of Sm-Fe alloy powder by reduction-diffusion process using new reductant of Li-Ca eutectic melt, AIP Adv. 13 (2) (2023) 025124, https://doi.org/10.1063/9.0000458.
[23] G. Qi, M. Hino, A. Yazawa, Experimental study on the reduction-diffusion process to produce Fe–Nd, Fe–Sm, Co–Nd and Co–Sm alloys, Mater. Trans., JIM 31 (6) (1990) 463–470, https://doi.org/10.2320/matertrans1989.31.463.
[24] A. Kawamoto, T. Ishikawa, S. Yasuda, K. Takeya, K. Ishizaka, T. Iseki, K. Ohmori, Sm$_2$Fe$_{17}$N$_3$ magnet powder made by reduction and diffusion method, IEEE Trans. Magn. 35 (5) (1999) 3322–3324, https://doi.org/10.1109/20.800512.
[25] G. Deng, Q. Jing, X. Wang, G. He, X. Ye, Synthesis mechanism of Sm$_2$Fe$_{17}$ alloy produced in reduction-diffusion process, J. Rare Earths 28 (2010) 420–424, https://doi.org/10.1016/S1002-0721(10)60357-2.
[26] S. Okada, K. Takagi, K. Ozaki, Direct preparation of submicron-sized Sm$_2$Fe$_{17}$ ultra-fine powders by reduction-diffusion technique, J. Alloys Compd. 663 (2016) 872–879, https://doi.org/10.1016/j.jallcom.2015.12.124.
[27] S. Okada, K. Suzuki, E. Node, K. Takagi, K. Ozaki, Y. Enokido, Preparation of submicron-sized Sm$_2$Fe$_{17}$N$_3$ fine powder with high coercivity by reduction-diffusion process, J. Alloys Compd. 695 (2017) 1617–1623, https://doi.org/10.1016/j.jallcom.2016.10.306.
[28] S. Okada, K. Suzuki, E. Node, K. Takagi, K. Ozaki, Y. Enokido, Improvement of magnetization of submicron-sized high coercivity Sm$_2$Fe$_{17}$N$_3$ powder by using hydrothermally synthesized sintering-tolerant cubic hematite, AIP Adv. 7 (5) (2017) 056219, https://doi.org/10.1063/1.4975052.
[29] S. Okada, E. Node, K. Takagi, Y. Fujikawa, Y. Enokido, C. Moriyoshi, Y. Kuroiwa, Synthesis of Sm$_2$Fe$_{17}$N$_3$ powder having a new level of high coercivity by preventing decrease of coercivity in washing step of reduction-diffusion process, J. Alloys Compd. 804 (2019) 237–242, https://doi.org/10.1016/j.jallcom.2019.06.385.
[30] J. Kim, H.-L. Wu, S. Hsu, K. Matsumoto, R. Sato, T. Teranishi, Nanoparticle approach to the formation of Sm$_2$Fe$_{17}$N$_3$ hard magnetic particles, Chem. Lett. 48 (9) (2019) 1054–1057, https://doi.org/10.1246/cl.190376.

[31] S Perry George, L.G. Macdonald, Role of $CaCl_2$ in the reduction of PuO_2, J. Nucl. Mater. 130 (1985) 234–241, https://doi.org/10.1016/0022-3115(85)90312-5.
[32] Chi-Jen Chen, Tin-Yu Liu, Ying-Chang Hung, Cheng-Hao Lin, Shou-Hsiung Chen, C.D. Wu, Effect of $CaCl_2$ and $NdCl_3$ on the manufacturing of Nd-Fe-B by the reduction-diffusion process, J. Appl. Phys. 69 (8) (1991) 5501–5503, https://doi.org/10.1063/1.347980.
[33] Y.-J. Cho, H.-C. Yang, H.-C. Eun, E.-H. Kim, I.-T. Kim, Characteristics of oxidation reaction of rare-earth chlorides for precipitation in LiCl-KCl molten salt by oxygen sparging, J. Nucl. Sci. Technol. 43 (10) (2006) 1280–1286, https://doi.org/10.1080/18811248.2006.9711221.
[34] S.M. Howard, Ellingham Diagrams, SD School of Mines and Technology, 2006.
[35] Thomas Degen, Mustapha Sadki, Egbert Bron, Uwe König, G. Nénert, The highscore suite, Powder Diffr. 29 (S2) (2014) S13–S18, https://doi.org/10.1017/S0885715614000840.
[36] N. Kawamura, T. Taniguchi, S. Mizusaki, Y. Nagata, T. Ozawa, H. Samata, Functional intermetallic compounds in the samarium–iron system, Sci. Technol. Adv. Mater. 7 (1) (2006) 46, https://doi.org/10.1016/j.stam.2005.11.004.
[37] J.-C. Yun, S.-M. Yoon, G.-Y. Lee, J.-P. Choi, J.-S. Lee, Microstructure and magnetic property of Sm_2Fe_{17} nanopowder synthesized by modified reduction-diffusion process, Mater. Trans. 55 (10) (2014) 1630–1633, https://doi.org/10.2320/matertrans.M2014152.
[38] X.-F. Xiao, P.-Z. Si, H.-L. Ge, C.-J. Choi, Preparation of Sm-Fe-N by high-pressure N_2 nitridation and Sm_2Fe_{17} by a diffusion process, J. Electron. Mater. 47 (2018) 7472–7475, https://doi.org/10.1007/s11664-018-6688-5.